

Dynamics of weakly evaporating and non-evaporating drops falling in air

Jorge Chavarria^a, Saúl Piedra^b, Guillermo Hernández-Cruz^a, Lilia Hernández-Sotelo^c,
Alfonso Castrejón-Pita^d, Eduardo Ramos^a

^a*Renewable Energy Institute,*

Universidad Nacional Autónoma de México, Temixco, 62580, Morelos, Mexico

^b*CONACyT-Centro de Ingeniería y Desarrollo Industrial, Queretaro, 76270, Queretaro, Mexico*

^c*ITESM, Xochitepec, 62790, Morelos, Mexico*

^d*Fluids Dynamics Laboratory, Department of Engineering Science,
University of Oxford, OX1 3PJ, UK*

Abstract

The dynamics of evaporating and non-evaporating drops falling in air under the influence of gravity is experimentally and theoretically studied in this work. Water and drops with diameters 2.0 and 2.7 mm and acetone drops 1.8 and 2.0 in diameter were tracked for approximately 2 m, corresponding to a flight-time of almost one second; at the end of the observation region, in most cases, the drops reached velocities $\sim 80\%$ terminal velocity. Vertical positions of falling drops as a function of time and horizontal positions at different heights were recorded. Initially, the motion of non-evaporating water drops was rectilinear with a remarkable reproducibility in all experimental runs, showing narrow standard deviations in their horizontal position. When the increasing Reynolds numbers reached approximately 700, trajectories of individual drops diverged from each other. This effect may be attributed to the laminar-turbulent transition of the drops wake. It was also observed that the spatial dispersion, along horizontal cuts along their fall, evolved from a narrow to a wider monomodal distribution to bimodal one as the traveled distance increases. The acetone drops evaporated as they fall and although their velocity increased, the diameter reduction prevented the drops from reaching the critical transition Reynolds number, maintaining the dispersion in the horizontal positions relatively narrow. A maximum volume loss due to evaporation of 13% is recorded at the lower end of the observation region. Simplified theories based on the drag coefficients of fixed spheres closely predict the drops vertical positions as a function of time, for both evaporating and non-evaporating drops. Calculations based on heat and mass transfer correlations for fixed spheres show a satisfactory agreement when compared with the experimental observations of the radii of evaporating drops as a function of time.

1. Introduction

The dynamics of evaporating and non-evaporating drops has attracted attention due to its importance in a variety of fields, such as in meteorology [1], combustion research [2] and, more recently, inkjet printing [3]. In the context of renewable energies, the

Preprint submitted to Elsevier

April 11, 2022

Nomenclature

A	drop effective area (m^2)
A_s	drop surface area (m^2)
C	specific heat capacity of acetone (J/kg K)
C_d	Drag coefficient
c_s	saturated concentration at the temperature of drop surface (kg/m^3)
c_∞	saturated concentration far away from the drop (kg/m^3)
D	vapor diffusivity (m^2/s)
d	diameter of the drop (m)
Eo	Eötvös number, $g\Delta\rho d^2/\sigma$
g	gravity acceleration (m/s^2)
h	heat transfer coefficient ($\text{W/m}^2\text{K}$)
h_m	mass transfer coefficient (m/s)
k	thermal conductivity (W/m K)
L	Latent heat (J/kg)
m	drop mass (kg)
Mo	Morton number, $g\mu^4\Delta\rho/\rho^2\sigma^3$
Nu	Nusselt number, hd/k
Pr	Prandtl number, $\mu C_p/k$
p_s	saturated pressure (Pa)
R	vapor constant, R_o/μ_a
Re	Reynolds number, $\rho w d/\mu$
Re_T	terminal Reynolds number, $\rho w_T d/\mu$
R_o	Universal gas constant ($\text{kg m}^2/\text{K mol s}^2$)
Sc	Schmidt number, $\mu/\rho D$
Sh	Sherwood number, $h_m d/D$
T	temperature of the drop (K)
T_∞	temperature far away from the drop (K)
t	time (s)
w	vertical velocity (m/s)
w_T	vertical velocity (m/s)
x	horizontal coordinate (m)
y	horizontal coordinate (m)
z	vertical coordinate (m)

Greek symbols

$\Delta\rho$	difference between the densities of liquid and air
γ	Liquid-to-gas density ratio, ρ_l/ρ
μ	dynamic viscosity of air (Pa s)
μ_a	molar mass of acetone (kg/mol)
ν	kinematic viscosity of air (m^2/s)
ρ	density of the air (kg/m^3)
ρ_l	density of the drop (kg/m^3)
σ	surface tension coefficient (J/m^2)

accelerated evaporation of drops falling in air occurs in energy towers [4]. This phenomenon shares some important characteristics with the related topic of rigid spheres falling through a still fluid, where a vast body of knowledge is available. This analogy is especially valid when the surface tension is dominant over the dynamic stresses, allowing the assumption that drop deformations play a minor role in the general dynamics. The qualitative features displayed by the motion of non evaporating falling drops can be described in terms of the Eötvös number (EO), the Morton number (Mo), and the liquid-to-gas density ratio γ . For formal definitions and ranges explored in this study, see Section 3.1. The instantaneous velocity of drops is conveniently given in terms of the Reynolds number (Re). Two kind of forces are present in this phenomenon; force due to gravity which is independent of the dynamics, and the aerodynamic forces that arise from the nonzero relative velocity between the drop and the surrounding air. In turn, the latter can be divided into added mass and viscous forces. For water and acetone drops falling in air where $\gamma \gg 1$, the dynamics can be greatly simplified as the added mass is negligible and the interaction between the moving drop and the air can be described in the reference frame traveling with the drop. Moreover, as indicated by Michaelides [5], even though the actual motion of the drop is accelerating, the flow around the drop is closely related to the steady state flow around a fixed sphere. These considerations are corroborated by the observations reported here. The aerodynamic forces tend to deform the drops, flattening the front. However, according to Ern et al. [6], this effect is small for $Mo < 2.6 \times 10^{-11}$ and $EO < 1$ which is the case in the present work. The flow around a fixed, rigid sphere as a function of the Reynolds number can be summarized as follows: The creeping flow observed at Reynolds numbers smaller than 20 evolves into a stable axisymmetric pocket of vorticity that forms in the rear part of the sphere withing a range of Reynolds numbers: $20 < Re < 130$. The length of the vortical region forming the wake increases as the Reynolds number increases. According to Taneda [7] and Sakamoto and Haniu [8], the wake becomes unstable for Reynolds numbers larger than 130 but Wu and Faeth [9], found that it remains steady and axisymmetric up to $Re \sim 210$. The linear stability analysis of Natarajan and Acrivos [10], and the numerical calculations of Tomboulides and Orzag [11], indicate that at $Re = 210$, the wake loses axisymmetry to the first azimuthal mode and a wake is developed by the shedding of two thread vortices of opposite sign. This flow has a planar symmetry around a plane that contains the axis of symmetry and whose precise orientation is random. A transition leading to time-dependent flow is observed at approximately $Re = 280$. In the interval $300 < Re < 700$, the wake structure is formed by a sequence of interconnected vortex loops (hairpin vortices) that are periodically shed, with a weak but monotonically increasing dependence of the shedding frequency on the Reynolds number. Near the lower limit of the interval, the wake displays planar symmetry and according to the experimental observations of Sakamoto and Haniu [8] and numerical calculations of Tomboulides and Orzag [11], at a Reynolds number close to 500, the frequency of the vortex emission becomes irregular and the planar symmetry is lost. The numerical calculations also indicate that the vortices separation points on the surface of the sphere slowly rotate and consequently, the hairpin vortex structure of the wake is distorted, leading to a complicated wake pattern but in absence of small-scale structures. For Reynolds numbers exceeding 700-800, smaller structures in the form of second generation hairpin vortices appear in the wake and a more chaotic flow is observed behind the sphere. The origin of this phenomenon is attributed to a Kelvin-Helmholtz instability in the shear layer de-

tached from the boundary layer at the surface of the sphere. Another qualitative change in the dynamics of the wake occurs within this range of Re numbers. At approximately $Re = 700$, the vortex shedding frequency as a function of the Reynolds number displays a clear change in slope, going from an almost constant value to a much steeper function. This observation has been reported by numerous authors and is compiled by Achenbach [12]. Although a great deal of effort has been devoted in recording and calculating the wake structure and emission frequency of vortices, available information on the forces distribution on the surface of the sphere is scarce for non-axisymmetric flows.

The drag coefficient (C_d) that results from the interaction between the drop and the surrounding air is a complex function of the Reynolds number. Several empirical formulations containing properties that make them useful for specific applications are available in the literature. For instance, Morsi and Alexander [13] developed a second-order polynomial on the inverse of the Reynolds number that permits the integration of the equation of motion to obtain analytical expressions for the position and velocity of a falling sphere as a function of time. Also, a useful correlation accurate for $0 < Re < 1000$ obtained through direct fit to experimental data was reported by Mikhailov and Silva Freire [14]. The dynamics of evaporating falling drops share many features with the non-evaporating case. However, an obvious consequence of evaporation is a reduction in the diameter of the drop as it travels; this key difference must be incorporated into the analysis. Assuming that the evaporation process is diffusive, the drop diameter reduction is a function of the difference between the vapor concentration far away from the drop and the equilibrium vapor concentration at its surface. Moreover, evaporation generates temperature changes in the drop; however, when the drop and the air have different velocities, the drop heat and mass exchange is dominated by convection. Under these circumstances mass, momentum, and energy transfer, are all coupled. Convective drop evaporation has been intensively studied in the context of the physics of rain and combustion. Nevertheless, in most studies the focus of interest is bound to drops moving at constant velocities because the terminal velocity of raindrops is reached in only a few meters. The studies of Pruppacher and Klett [15] or Ludlam [16] offer a detailed discussion of drop dynamics in the context of meteorology, where other phenomena such as coalescence and break-up are also taken into account. Based on dimensional analysis, Frössling suggested that the convective non-dimensional mass transfer coefficient should be a function of the product $Re^{1/2}Sc^{1/3}$, where Sc corresponds to the Schmidt number [17]. Downing [18] experimentally corroborated this expression by exposing fixed drops (of a variety of liquids, including water and acetone) to constant air flows. While there is a general agreement (correct trend is followed) with the empirical correlation for convective mass transfer, it is important to emphasize that the dispersion of experimental data prevents an accurate specification of the numerical coefficients in the Frössling expression. It is well established in standard textbooks, such as that by Incropera et al. [19], that it is possible to assume a direct analogy between the heat and mass transfer equations. Therefore, the convective heat transfer coefficient can be expressed in a similar way to the mass transfer coefficient, with the Prandtl number replacing the Schmidt number.

In the present study attention is focused on the initial motion where the change in velocity is a dominant effect in the dynamics, in contrast to most previous studies where the emphasis is on the dynamics of drops once they have acquired their terminal velocity. Moreover, the possibility of drop evaporation is also considered; this phenomenon results

in a reduction of the drop diameter, consequently affecting the motion of the falling drop. Given the small diameters of drops used in the experiments reported here, drop deformation plays a minor role in the dynamics.

2. Experimental setup and methodology

The experimental rig consists of a 6 cm in diameter and 2 m long transparent soda lime glass tube with circular cross section, fixed in a vertical position by a rigid acrylic frame. The ends of the tube are open and at the top end, centered along its axis of symmetry, a computer-controlled drop dispenser [20] is placed.

The nozzle is a stainless steel tube with external and internal diameters of 0.41 mm and 0.2 mm respectively. A volumetric flow of $4.2 \times 10^{-9} \text{ m}^3/\text{s}$ generated one drop per second. With this frequency, the drops have zero initial velocity at the nozzle. The lower end of the tube is 50 cm above the floor. The images of the drops were captured with a Phantom Miro C110 high-speed camera mounted on a vertical rail, such that it can be fixed at different axial positions. The camera is located 4 cm away from the tube wall. For a CCD sensitive area of 1280×200 pixels, the camera records snapshots at speeds of up to 4400 frames per second. A lens (Computar 8 mm) was used which provided a field of view of 128 mm in the vertical direction and 20 mm in the horizontal direction. Background illumination was provided by a set of two rows of ten 20W LEDs, located opposite to the camera. A uniform illumination was obtained by placing a diffuser screen between the light source and the tube.

The methodology to capture the positions of individual drops as a function of time was as follows. Chains of drops were generated, and their images were captured by the high-speed camera. In the uppermost camera position, where the nozzle is in the field of view, up to 350 images of a falling drop are taken. The camera is then lowered to the next station, located 10 cm below the preceding position; this procedure was repeated 12 times. The images of drops were captured in windows 12 cm-long in the vertical direction. Observations from two consecutive stations are then concatenated with 2 cm overlapped information which contain up to 10 images, in order to obtain the trajectory of droplets along the full length of the system. The total distance recorded is 1.56 m. Drop images are less than one diameter away of each other in subsequent frames for all the vertical locations of the camera. The memory of the camera allowed runs of up to 20 drops. A sketch of the experimental setup is shown in Figure 1(a). The radius of the evaporating drop as a function of vertical position was obtained with a similar experimental setup as described in Figure 1(a), but in this case, the images of individual drops are larger ($46 \text{ pixels} \times 46 \text{ pixels}$) to increase the spatial resolution of the camera to better resolve the drop geometry, with the adverse result of reducing the size of the field of view. The images post-processing included finding the ellipse that best fitted the edge of the binarized drop image and the determination of its centroid. Also, care was taken to discard out-of-focus images to avoid drop size overestimation. A second method was devised to record the horizontal position of the drops at various vertical stations along their trajectory. The camera, was placed under the lower end of the tube, facing upwards. The positions of individual drops were then detected by illuminating a horizontal plane with a laser-sheet (LJK, 200 mW and 532 nm). As drops cross the illuminated plane, the camera records their position as bright spots. The laser-sheet was subsequently placed at 12 vertical stations separated 10 cm from each other, starting 60

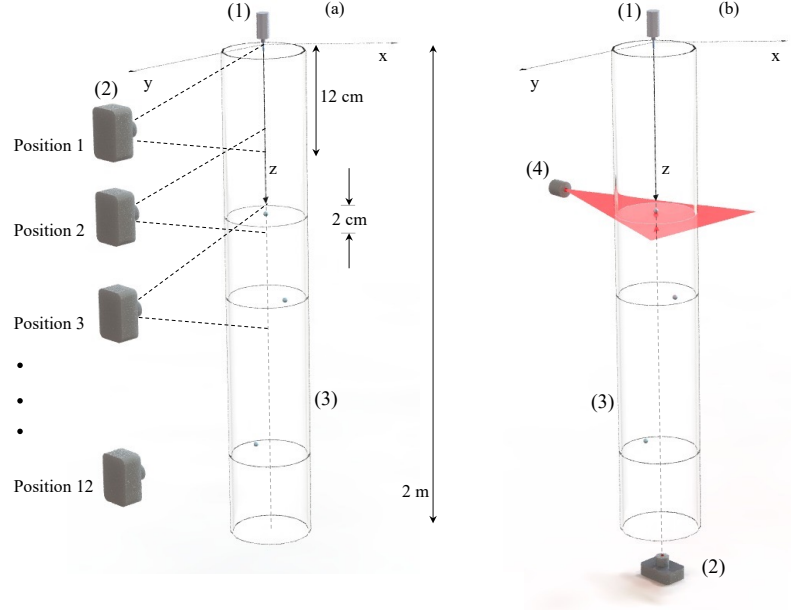


Figure 1: Experimental set up. (a) Arrangement used to detect the position of drops as a function of the vertical coordinate. (b) Arrangement used to detect the positions of drops in horizontal planes located at 12 vertical distances from the nozzle. (1) Drop dispenser, (2) High speed camera (3) Glass tube, (4) Laser light source.

cm from the top-end of the tube to detect the horizontal positions along the whole length of the tube. Typically, an individual drop image forms areas of 2×2 and 8×8 pixels in the positions further away and closer from the camera respectively. The positions of the drops are defined by the centroids of the images. On average, 80 events were recorded for each vertical position. A sketch of this experimental setup is shown in Figure 1(b).

3. Theoretical remarks

3.1. Nondimensional parameters

The qualitative features of the motion of non evaporating falling drops can be described in terms of the following three dimensionless parameters. a) The Eötvös number, $Eo = g\Delta\rho d^2/\sigma$ which compares the effects of gravity and surface tension, b) The Morton number $Mo = g\mu^4\Delta\rho/\rho^2\sigma^3$ that relates the effect of gravity, inertia and viscosity to the surface tension, and c) the liquid to air density ratio $\gamma = \rho_l/\rho$. In the previous expressions, g is the gravity acceleration, $\Delta\rho = \rho_l - \rho$ is the difference between the densities of liquid and air, d represents the diameter of the drop, σ corresponds to the surface tension coefficient and μ is the dynamic viscosity of air. Under the conditions of interest, $g = 9.81 \text{ m/s}^2$, $d \sim 2 \times 10^{-3} \text{ m}$. For water drops, $\Delta\rho = 997 \text{ kg/m}^3$, $\sigma = 72 \times 10^{-3} \text{ J/m}^2$, $\mu = 10^{-3} \text{ Pa s}$, while for acetone drops, $\Delta\rho = 791 \text{ kg/m}^3$, $\sigma = 2.37 \times 10^{-3} \text{ J/m}^2$, $\mu = 0.32 \times 10^{-3} \text{ Pa s}$. The motion of the drop is conveniently described in terms of the Reynolds number $Re = \rho w d / \mu$ where w is the instantaneous velocity. A closely related,

	water $d=2\text{mm}$	acetone $d=1.8\text{mm}$
Eo	0.54	1.06
Mo	2.6×10^{-11}	9.77×10^{-12}
γ	997	791
Re_T	830	536

Table 1: Dimensionless parameters for water and acetone drops. Eötvös number (Eo), Morton number (Mo), density ratio (γ). Terminal Reynolds number (Re_T).

useful parameter is the terminal Reynolds number (Re_T) which is based on the terminal velocity of the drop and therefore time-independent. The numerical values of the parameters for the conditions of interest are given in Table 1. The dynamics of a drop as it falls in air is conveniently described in terms of the drag coefficient (C_D) which represents the aerodynamic forces in non-dimensional form and is a function of the Reynolds number. When evaporation is taken into account, two extra non-dimensional numbers are required, the mass and thermal energy transfer coefficients, namely the Sherwood and Nusselt numbers, denoted as Sh and Nu , respectively. Given that the mass and heat exchanges take place under convective conditions, these parameters depend on the relative velocity between the drop and the surrounding air (Re) and are not externally fixed.

3.2. Dynamics of non-evaporating falling drops

The falling motion of a drop represents a complicated phenomenon due to the interplay of different effects in the two-way coupling between the deformable body and the surrounding fluid. The dimensionless parameters listed in Table 1 indicate that the drops used in the experimental observations will show only slight departures from spherical shapes [21], and that the internal motion will have no impact on the overall dynamics [22]. Here, simplified models that will guide the interpretation of experimental observations are briefly described.

A simple model to describe the dynamics of a non-deformable sphere falling under the action of gravity in an incompressible fluid is based on the momentum balance that includes gravity and a drag force. Namely,

$$m \frac{dw}{dt} = C_D \rho w^2 A - mg, \quad (1)$$

where w , m and ρ are the vertical velocity, mass and density of the sphere respectively, and A is its effective area. The acceleration of gravity is represented by g and the drag coefficient by C_D . The added mass term has been omitted in the previous expression because $\gamma \sim 10^3$. Also, the drag coefficient in the accelerated motion is assumed to be equal to the drag of a fixed sphere interacting with a constant-velocity incoming flow. The drag coefficient is a function of the velocity or equivalently, of the Reynolds number (Re). Several expressions that approximate the function $C_D(Re)$ are available in the literature in the range of Reynolds number of interest. See [22], [13], [14] and references therein. The expression of Mikhailov and Silva Freire [14] (shown and commented in the Appendix) is used in the present work. Equation (1) along with the expression for the drag coefficient was integrated numerically to obtain the velocity as a function of

time using a 4th order Runge-Kutta method. Once the velocity has been calculated, the instantaneous vertical position of the drop was obtained by integrating the expression

$$z = \int_o^z w(\tau) d\tau. \quad (2)$$

For future reference, it is observed that according to the simplified model, the terminal velocity for a drop of 2 mm in diameter is 6.5 m/s, and the corresponding terminal Reynolds number is $Re_T = 840$ which is in good agreement with the experimental data [23]; see also [24]. The distance and flight-time required to reach 99% of the terminal velocity for a drop 2 mm in diameter are 10.7 m and 2.5 s respectively.

3.3. Dynamics of evaporating falling drops

The simplified model presented in the previous subsection can be generalized to include evaporation. The momentum equation describing the dynamics is as follows,

$$\frac{d(mw)}{dt} = C_D \rho w^2 A - mg \quad (3)$$

or

$$m \frac{dw}{dt} = C_D \rho w^2 A - mg - w \frac{dm}{dt}. \quad (4)$$

The evaporation rate dm/dt can be expressed as

$$\frac{dm}{dt} = A_s h_m (c_s - c_\infty), \quad (5)$$

where h_m is the mass transfer coefficient per unit area and c_s and c_∞ are the saturated concentration at the temperature of the surface of the drop and the concentration far away (infinity), respectively. The surface area of the drop A_s is related to the effective area by $A_s = 4A$. The mass transfer coefficient h_m can be obtained using the Frössling correlation that associates the Sherwood number Sh (dimensionless h_m) to the Reynolds and Schmidt¹ (Sc) numbers [17]:

$$Sh = \frac{h_m d}{D} = 2.0 + 0.552 Re^{1/2} Sc^{1/3}. \quad (6)$$

In the previous equation, D corresponds to the vapor diffusivity. For acetone, the vapor diffusivity in air is equal to $12.5 \times 10^{-6} \text{ m}^2/\text{s}$ [25].

The vapor concentration at the surface of the drop depends on the drop temperature and can be calculated assuming that the vapor is an ideal gas as:

$$c_s(T) = p_s / RT, \quad (7)$$

where p_s is the saturated pressure at temperature T and R is the vapor constant defined by $R = R_o / \mu_a$. Where $R_o = 8.31446 \text{ kg m}^2 \text{ K}^{-1} \text{ mol}^{-1} \text{ s}^{-2}$ is the universal gas constant

¹The Schmidt number is defined as the ratio of viscous to mass diffusion

and $\mu_a = 58.08 \times 10^{-3}$ kg/mol is the molar mass of acetone. The saturated pressure can be calculated with the Clausius-Clapeyron equation or with the simpler, yet accurate expression known as Antoine equation,

$$\ln_{10} p_s = a - \frac{b}{c + T}. \quad (8)$$

For acetone, $a = 4.42448$, $b = 1312.25$ and $c = -32.745$. The temperature should be expressed in Kelvin and the pressure in bars (10^5 Pa) [26].

Solvent evaporation results in a change in the temperature of the drop. Thus, this modifies the saturated concentration according to equations (7) and (8). The temperature of the drop can be calculated considering the energy conservation in the drop. Assuming that the temperature of the drop can be characterized by a single value, the energy balance is:

$$mC \frac{dT}{dt} = -hA_s(T - T_\infty) - L \frac{dm}{dt}, \quad (9)$$

where $L = 534 \times 10^3$ J/kg is the latent heat and $C = 2.14 \times 10^3$ J/kg K is the specific heat capacity of the acetone; h is the heat transfer coefficient per unit area and T_s and T_∞ are the temperature at the surface of the drop and at infinite, respectively. The heat transfer coefficient h can be obtained using the Ranz and Marshall correlation that relates the Nusselt number Nu (nondimensional h) to the Reynolds and the Prandtl (Pr) numbers [19] where:

$$Nu = \frac{hd}{k} = 2.0 + 0.6Re^{1/2}Pr^{1/3}. \quad (10)$$

In the previous expression, $k = 0.18$ W/m K is the thermal conductivity of acetone.

Equations (4), (5), and (9) are numerically integrated using a 4th order Runge-Kutta method to get the velocity, mass and temperature of the drop as a function of time. Given that the density can be considered constant, it is more convenient to convey the mass loss as the radius of the drop in a time-dependent expression.

Figure 2 shows the radius, the vertical velocity and the temperature as a function of time for drops of water and acetone with 2 mm in diameter moving in air at a temperature of 298 K and pressure of one atmosphere. The concentrations of water and acetone are zero when considering long distances. The time frame chosen for the analysis is 14 s which is slightly longer than the time required for total evaporation of the acetone drop. In this interval, the radius of the water drop remains practically constant, while the radius of the acetone drop displays a linear reduction during most of the process. The vertical velocity shows a maximum for both, water and acetone, but given that the acetone is more volatile, the maximum is reached sooner. After the maximum, the velocity drops monotonically to zero at total evaporation. In the time interval explored, the water drop has a velocity close to the terminal velocity of a non evaporating sphere (6.4 m/s) with a shallow maximum at 2.5 s. The total evaporation time for the water drop under these conditions is greater than 2 minutes. The maximum velocity reached by the acetone drop is 5.3 m/s at $t = 1.5$ s. The temperature of the water drop remains practically constant which is consistent with the small reduction of the drop radius. The time evolution of the acetone drop temperature displays three zones. Initially, the temperature shows a

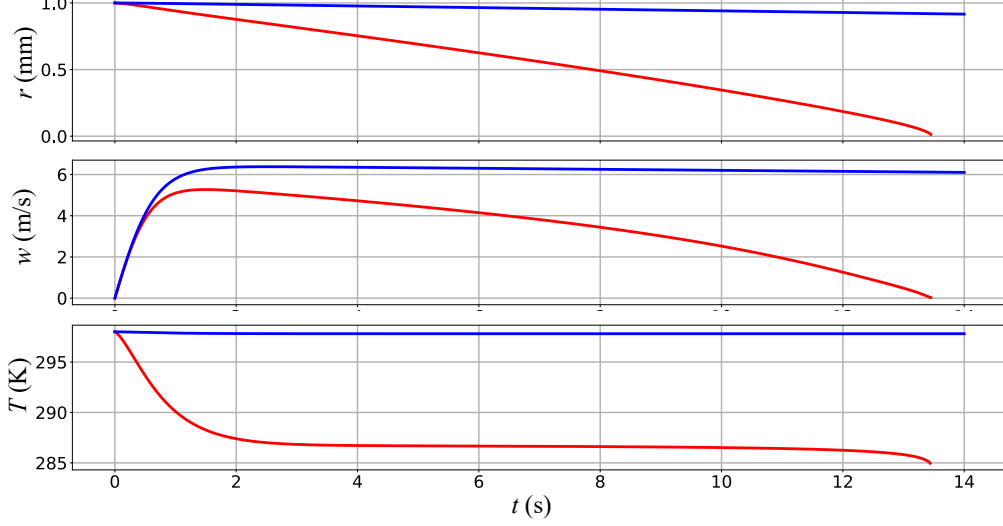


Figure 2: Upper panel, radius; middle panel, vertical velocity; and lower panel, temperature as a function of time for 1mm-radius water (blue line) and acetone (red line) drops falling in air. No vapor is present far away from the drops.

relatively large temperature decrease in a time span that roughly corresponds to the accelerating phase of the dynamics. The temperature reduction rate is much smaller when the drop decelerates. In the last few seconds the temperature suddenly drops fast as total evaporation is reached. As explained in detail in the next section, it is noted here that the maximum time for the experimental observations is 0.78 s.

4. Experimental observations

4.1. Vertical drop positions

4.1.1. Non-evaporating drops (water)

Experimentally acquired positions of 2.0 ± 0.02 mm diameter water drops as a function of time, together with the trajectory predicted by the model described in the previous section (Equation 1) are shown in Figure 3. As mentioned in Section 2, observations were taken every 10 cm with observation windows 12 cm in height. The ambient relative humidity is 24% and the estimated time scale from the theoretical model for total evaporation is 130 s. Given that the flight time is less than one second, it can be considered that the drop does not lose mass in the whole descending motion.

The color line segments in Figure 3(a) represent the positions of drops as a function of time extracted from the video images. Observations just after the drops are released at the nozzle indicate that the initial velocity is zero. Each segment represents independent observations at subsequent heights, and their smooth concatenation provides evidence of the repeatability of successive measurements. Trajectories of 191 drops (600 to 84 snapshots depending on the velocity of the drop) were used to build the graph. See Section

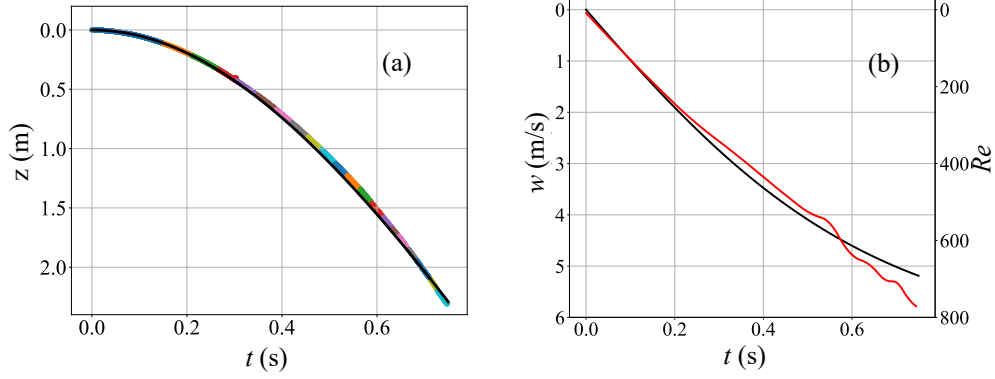


Figure 3: (a) The color line segments are the experimental positions of the drop as a function of time for 2.0 mm diameter water drops. The distance increases downwards and the origin of coordinates is at the nozzle. The continuous black line corresponds to the position of a sphere in free fall with the drag coefficient calculated with equation (1). (b) Velocity as a function of time. The red line represents the derivative of the experimental positions shown in (a), and the black line is the velocity given in equation (1). The instantaneous Reynolds number is given on the right vertical axis.

2 for details on the experimental methodology. The black line is the vertical position of drops predicted by the theory described in Section 3.2; the agreement between the experimental observations and the simplified theory is very good. This further indicates that the drag force on the drop is accurately predicted by the drag coefficient of a fixed sphere, as it is expected for $\gamma \gg 1$ [5]. Also, it is concluded that as far as the dynamics is concerned, the surface of the drop is rigid and nonslip boundary condition may be valid. In the time interval $0.05 \text{ s} < t < 0.065 \text{ s}$, the theoretical prediction slightly overestimates the position. The small discrepancy is probably due to the deformation of the drop due to the increased pressure at the front. In Figure 3 (b), the velocity of the drop predicted by the solution to equation (1) is shown in black and the time derivative of the cubic spline interpolation of the experimental data is shown in red. As expected, the agreement is also good, but the theoretical-experimental agreement deteriorates at the end of the observations. This effect may be attributed to the irregularity of the motion due to the transition to a turbulent wake. This point will be discussed in more detail in Section 4.2. Note that the terminal velocity of a 2 mm drop is 6.4 m/s [23], and therefore the drop has reached 81% of its terminal velocity at the end of the observation.

4.1.2. Evaporating drops (acetone)

Experimental observations of the positions of a $1.8 \pm 0.03 \text{ mm}$ diameter acetone drops as a function of time are shown in Figure 4(a) as a line formed by sequential colored line segments. In the same plot, the black and red lines represent the positions calculated with equations (1) and (4), respectively. As it may be appreciated, the match is very good for most of the trajectory, with the largest discrepancies in the region far away from the nozzle. To highlight the differences, the instantaneous position difference normalized with the drop diameter ($\Delta z/D$) is shown in Figure 4 (b). As it may be appreciated, the

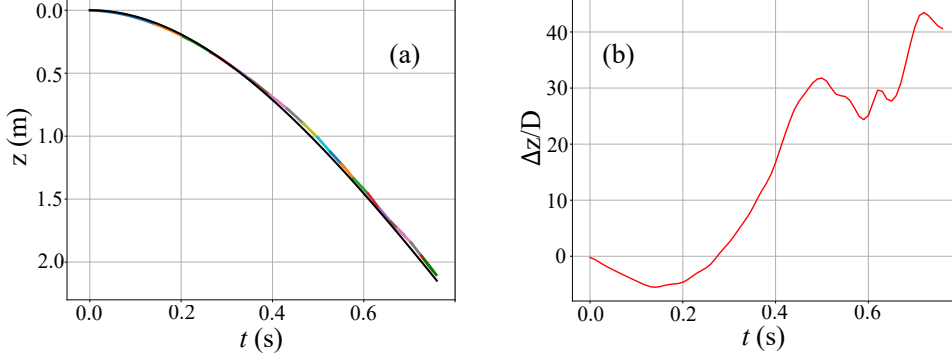


Figure 4: (a) Experimental positions as a function of time for 1.8 mm diameter acetone drops. The color line segments correspond to the experimental data for evaporating drops. The black line is equation (4). (b) Instantaneous position difference between the experimental observations and equation (4).

positions calculated considering mass loss give a better fit. This results confirm that the quasi-steady assumption to incorporate the steady drag and mass transfer expressions yield satisfactory agreement. At this point, it is important to comment that for the observed conditions the theoretical curves for evaporating and non-evaporating drops are very similar making it difficult to assess the importance of the evaporation effects in the model.

In order to detect the volume reduction due to evaporation, observations were made using acetone drops with a diameter of 1.80 ± 0.03 mm. Images of a collection of images ranging from 35 to 80 drops were captured by placing the camera at six vertical positions, as explained above. The vertical size of the observation windows (field of view) was fixed to fit at least six drop diameters. The shape of the drops vary slightly as they fall, and the volume was calculated assuming that they were ellipsoids. Figure 5 shows the volume of drops as a function of time. The uncertainty bar is the standard deviation of observations at a specific position of the camera. The volume calculated with the theory of Section 3.3 correctly predicts the qualitative trend but the evaporation slightly underestimated. This is consistent with the results shown in Figure 4. In the last observation window, it is found that the radius is reduced by 4.5%, which corresponds to a volume loss of 13%.

4.2. Drop distributions in horizontal planes

The vertical motion is the dominant effect on the drop dynamics, but due to aerodynamic forces generated in the boundary layer formed around the drops, horizontal displacements occur. The horizontal positions of drops are detected using the experimental rig described in Section 2 and illustrated in Figure 1(b). In the present analysis, water drops 2.7 mm in diameter are studied. These drops are slightly larger than the ones used in the study described in the previous paragraph as this allows us to explore a wider range of Reynolds numbers. Acetone drops used were 2.0 mm in diameter.

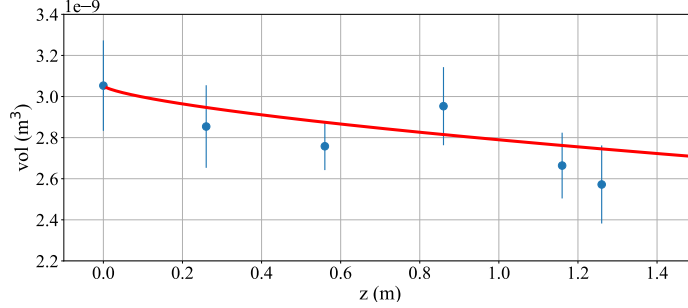


Figure 5: Blue dots represent drop volume as a function of position for evaporating acetone drops. The uncertainty bars are the standard deviations. The last observation at 1.26 m indicates that the drop lost 13% of its initial volume. The red line is the radius from the theory given in Section 3.3.

4.2.1. Non-evaporating drops (water)

Shortly after a drop is released, its velocity increases continuously and its trajectory is vertical. Then, at a critical Reynolds number, forces resulting from the dynamic interaction between the drop and the surrounding gas push the drops horizontally. It is found that there is no preferred direction in the horizontal plane and hence the trajectories of different drops diverge. These features are shown in the sample distributions of A, B and C horizontal planes in Figure 6 for water drops 2.7 mm in diameter. In this figure the arbitrary orientation of the x, y coordinate axes are also given. As the drops descend, the standard deviation of the x and y position distributions widen and the center of the intercept distribution separates from the vertical. At approximately the distance of 1.34 m (plane D), the y-distribution becomes bi-modal. This feature is also found at lower planes. A more complete collection of observations is given in Figure 7 where the positions of the drops distributions in the (x,z) and (y,z) planes are shown. From this figure it can be seen that the rectilinear motion extends from the release point to approximately $z = 0.7$ m which corresponds to $Re = 600$, where a small departure from the vertical motion is seen up to 1.1 m ($Re = 780$). Then, a larger drift in the horizontal plane is observed with the bi-modal distributions occurring after $z > 1.3$ m. The Reynolds number where the first departure from the vertical motion is observed is close to the Reynolds number ($Re = 500$) at which the wake of a fixed sphere starts oscillating with irregular frequencies, but without small scale motions as described by Tomboulides and Orzag [11] and Sakamoto and Haniu [8]. For the second observed transition (after 1.1 m), the Reynolds number approximately coincides with the Reynolds number ($Re = 800$) where the formation of small scale vortices leading to a turbulent wake was observed by Sakamoto and Haniu [8], and also with the increase of vortex shedding frequency reported by Achenbach [12].

4.2.2. Evaporating drops (acetone)

A similar analysis to the one described in the previous paragraph was carried out using acetone, which under the laboratory conditions evaporated more rapidly than water. Drops with an initial diameter of 2 mm are used. The results are shown in Figure 8. In the evaporating case, it is also observed that near the nozzle ($z < 0.75$ m), most of the

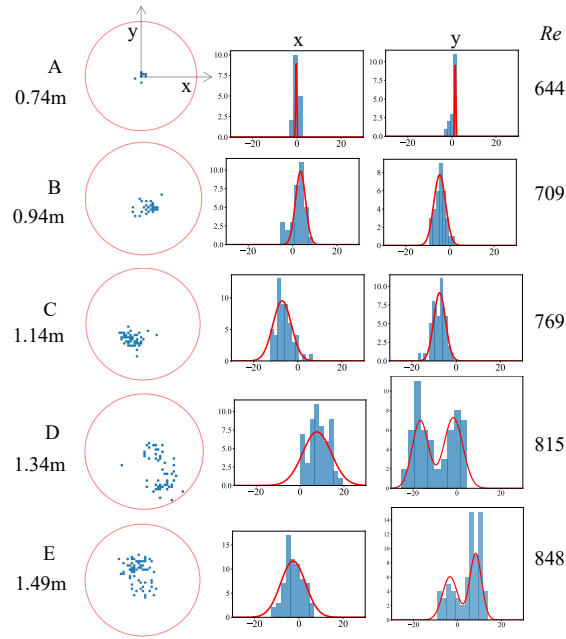


Figure 6: Positions of the centroids of water drops of 2.7 mm in diameter in horizontal planes located at sample distances from the nozzle. The circles in the first column show the polar distributions of the intercepts of the trajectories with the horizontal planes. The last two columns show the histograms and the Gaussian fits of the intercept positions along the (arbitrarily oriented) x and y coordinates respectively.

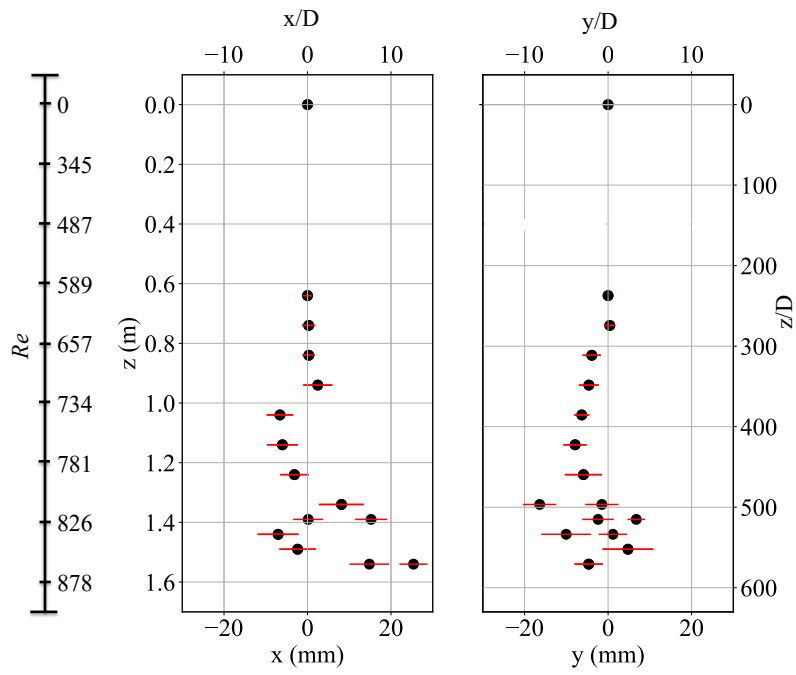


Figure 7: Left panel: Positions of the centroids of water drops distributions in the (x, z) plane. Right panel: positions in the (y, z) plane. Notice the different scales in the vertical and horizontal directions. The red horizontal bars represent the standard deviations of the position distributions. The Reynolds number is shown on the left bar.

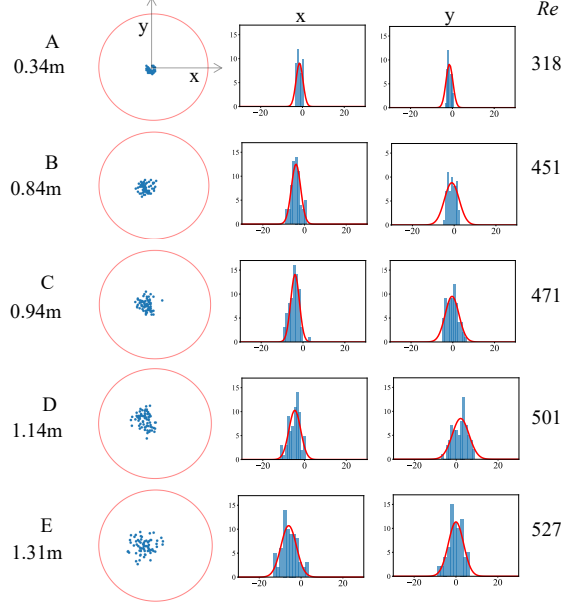


Figure 8: Positions of the centroids of acetone drops in horizontal planes located at sample distances from the nozzle. The circles in the first column show the polar distributions of the intercepts of the trajectories with the planes. The last two columns show the histograms and the Gaussian fits of the intercept positions along the (arbitrarily oriented, see Figure 1) x and y coordinates respectively.

drops follow a vertical path and that the dispersion increases with the distance. However, in contrast with the non-evaporating case, the dispersion of the intercepts is always mono-modal and the horizontal drift is smaller. It is interesting to note that due to the reduction in diameter, the largest Reynolds number attained is approximately 500 and probably the wake developed irregular oscillations, but no small structures leading to a turbulent wake were generated as it is the case in the non-evaporating case. The dynamical behavior just described is better documented in Figure 9 where the trajectory is shown in the (x,z) and (y,z) planes. Please note the change in scale used in the horizontal directions axis which was required to highlight the deviations from the vertical.

5. Conclusions

Water drops with diameters in the range $2.0 \text{ mm} < d < 2.7 \text{ mm}$ and acetone drops ($1.8 \text{ mm} < d < 2.0 \text{ mm}$) were tracked for approximately two meters as they fall under the action of gravity; the observations reported in this manuscript correspond to almost one second of flight-time. The drops are video recorded and the vertical positions of their centroids are modeled with simplified theories. In the two cases explored, the liquid-to-air density ratio is very large and added mass does not contribute to the analysis. The vertical and horizontal positions of the drops were explored. The main conclusion regarding the analysis of the vertical motion is that the dynamics of water drops is closely predicted with a model that includes a drag coefficient corresponding to a fixed sphere

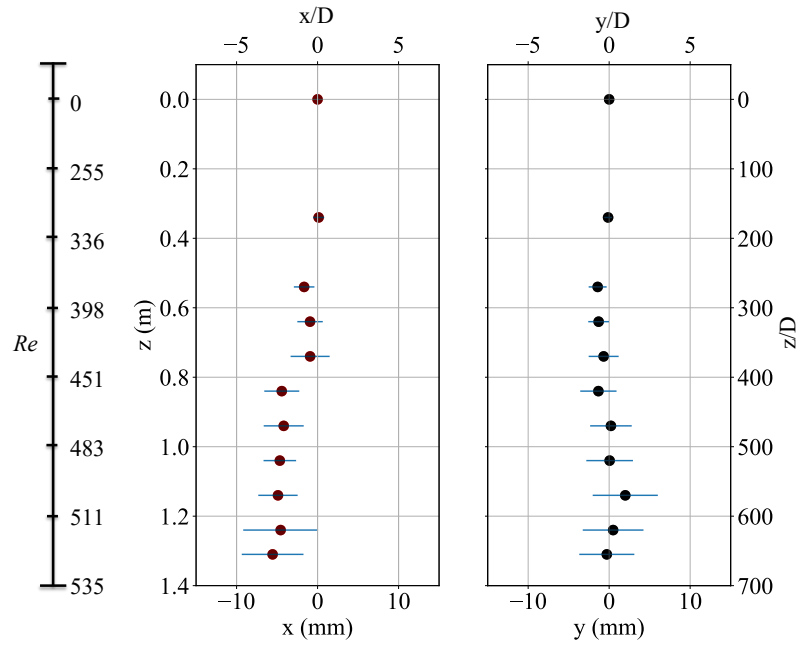


Figure 9: Observed positions of the centroids in horizontal planes of the distributions of acetone droplets at different distances from the nozzle. Left: positions in the (x, z) plane. Right: positions in the (y, z) plane. The horizontal bars represent the standard deviation of the distributions. The horizontal directions have been amplified to clearly show drift.

under a constant velocity incoming flow. The vertical positions predicted using a model that considers evaporation and adjusts the transport coefficients for the variable radii, agree well with the experimental results, but it must be emphasized that, within the explored region in parameter space, the differences between the evaporating and non-evaporating drops are small. Using the results obtained in the model, it is expected that the differences would increase substantially for larger observation windows. The analysis of the horizontal positions of drops along the travelled distance demonstrated that there is no preferred direction of motion in the horizontal direction, and hence the trajectories of different drops diverge due to forces that originate at the boundary layer in the vicinity of the drop; this generates a dispersion in the horizontal positions along the falling path. In the experiments with water drops, a departure from a rectilinear motion (observed immediately after their release) is detected when the drops reach approximately a Reynolds number of 400 which roughly corresponds to the Reynolds number $Re \sim 500$, when the wake of a fixed sphere sheds vortices with irregular frequency. The horizontal drift becomes more pronounced when the Reynolds number exceeds 700 which coincides with the Reynolds number where small vortical structures occur in the wake leading to a turbulent flow. In contrast, acetone drops follow almost rectilinear motions from the release point to approximately $z = 1.4$ m. The horizontal motion is detectable, but smaller than water drops. Crucially, as the drops evaporate, their reduction in their radii prevent them from reaching the critical Reynolds number for these effects to become apparent. The simplified theoretical model indicates that for acetone, the time for maximum velocity is 1.5 s which corresponds to a distance of 6 m and total evaporation time is 13.5 s (46 m). Using a more volatile substance, or a larger observation distance, it might be possible to observe the maximum velocity predicted by the theory and even total evaporation. This is the subject of an ongoing research. Our study contributes to understand fundamental phenomena in droplet dynamics which is relevant in several applications. For instance, in continuous inkjet printing (CIJ), due to the relatively long distances the drops need to travel to reach the substrate, the development of unsteady wakes and solvent evaporation may be playing a role in affecting both accuracy and final size and thus the footprint. In some CIJ applications you may have a $120 \mu\text{m}$ drop travelling at 30 m/s, resulting in a $Re \sim 400$, near the first regime transition where vortices start to be shed. Jets in internal combustion engines are a lot faster, and a milliard of drops of a wide range of diameters will be interacting with each other, which will affect both the concentration of solvent vapour and hydrodynamic interaction between these droplets. In direct injection internal combustion engines droplets may be injected at velocities of up to 300 m/s resulting in very high Reynolds numbers. Interaction among droplets and their vapours will result in an even more complicated dynamics. Our results may shed some light as to how each of these will behave individually, which could be incorporated into much more complex numerical simulations. The same is applicable in the dynamics of evaporating of respiratory droplets. Drops of up to 1mm are ejected at record speeds of 15 m/s during a cough, resulting in initial $Re > 1000$, well into the regimes where disturbances in their trajectories are expected. Water will eventually evaporate, aerosolising particles which may contain, among a milliard of components, virus and/or bacteria. Evidently, other important physical phenomena should be incorporated to build realistic models for specific applications.

Acknowledgements

JC acknowledges with gratitude the Ph.D. scholarship awarded by CONACYT (Mexico). SP conveys his special appreciation to the CONACYT Research Fellow Program (*Catedras* CONACYT). AAC-P acknowledges the support received from the Royal Society through a University Research Fellowship (No. URF\R\180016 with extension CEC19\100191) and an Enhancement Award (No. RGF\EA\181002). AAC-P, SP and JC further thank the Royal Society for the Newton Mobility Award No. NI170191, which enabled international cooperation and research exchanges. The initial stage of the project was partially funded by the Royal Academy of Engineering, via a Newton Research Collaboration Programme, award reference No. NRCP 1415/198.

Appendix

Based on the Shanks transform, Mikhailov and Silva Freire [14] suggest the following expression for the drag coefficient of a fixed sphere exposed to a uniform incoming flow as a function of the Reynolds number:

$$C_D = \frac{3808((1617933/2030) + (178861/1063)Re + (1219/1084)Re^2)}{681Re((77531/422) + (13529/976)Re - (1/71154)Re^2)}. \quad (11)$$

They report that the expression is valid for $1 < Re < 1000$ with differences with respect to experimental observations of 2.5% , 5.7% and 7.5% for $Re = 10, 100$ and 1000 respectively.

References

- [1] P. K. Wang, Physics and dynamics of cloud and precipitation, Cambridge University Press, 2013.
- [2] S. S. Sazhin, Modelling of fuel droplet heating and evaporation: Recent results and unsolved problems, *Fuel* 196 (2017) 69-101.
- [3] D. Lohse, Fundamental fluid dynamics challenges in inkjet printing, *Annual Review of Fluid Mechanics* 59 (2022) 349-382.
- [4] M. Bauer, I. Gasser, Modeling, asymptotic analysis, and simulation of an energy tower, *SIAM Journal on Applied Mathematics* 72 (2012) 362-381.
- [5] E. E. Michaelides, Particles, bubbles and drops. Their motion, heat and mass transfer, World Scientific, 2006.
- [6] P. Ern, F. Risso, D. Fabre, J. Magnaudet, Wake-induced oscillatory paths of bodies freely rising or falling in fluids, *Annual Review of Fluid Mechanics* 44 (2012) 97-121.
- [7] S. Taneda, Experimental investigation of the wake behind a sphere at low Reynolds numbers, *Journal of the Physical Society of Japan* 11 (1956) 1104-1108.
- [8] H. Sakamoto, H. Haniu, A study on vortex shedding from spheres in a uniform flow, *Journal of Fluids Engineering* 112 (1990) 386-392.
- [9] J.S. Wu, G.M. Faeth, Sphere wakes in still surroundings at intermediate Reynolds numbers, *AIAA Journal* 31 (1993) 1448-1455.
- [10] R. Natarajan, A. Acrivos, The instability of the steady flow past spheres and disks, *Journal Fluid Mechanics* 254 (1993) 323-344.
- [11] A.G. Tomboulides, S.A. Orszag, Numerical investigation of transitional and weak turbulent flow past a sphere, *Journal of Fluid Mechanics* 416 (2000) 45-73.
- [12] E. Achenbach, Vortex shedding from spheres, *Journal of Fluid Mechanics* 62 (1974) 209-221.
- [13] S. Morsi, A. Alexander, An investigation of particle trajectories in two-phase flow systems, *Journal of Fluid Mechanics* 55 (1972) 193-208.
- [14] M.D. Mikhailov, A.P. Silva Freire, The drag coefficient of a sphere: An approximation using Shanks transform, *Powder Technology* 237 (2013) 432-435.
- [15] H.R. Pruppacher, J.D. Klett, Microphysics of clouds and precipitation (Boston, MA: Reidel), 1978.
- [16] F.H. Ludlam, Clouds and storms. The behavior and effect of water in the atmosphere, Pennsylvania State University Press (1980).

- [17] N. Frössling, Über die Verdunstung fallender Tropfen, Gerlands Beitr. Geophys 52 (1938) 170-216.
- [18] C.G. Downing, The evaporation of drops of pure liquids at elevated temperatures: rates of evaporation and wet bulb temperatures, American Institute of Chemical Engineers Journal 12 (1966) 760-766.
- [19] F.P. Incropera, D.P. Dewitt, T.L. Bergman, A.S. Lavine, Fundamentals of heat and mass transfer, sixth ed., John Wiley & Sons, 2007.
- [20] Micro flow rate syringe pump. *Longer* Model TJ-2A/L0107-2A.
- [21] H.R. Pruppacher, K.V. Beard, A wind tunnel investigation of the internal circulation and shape of water drops falling at terminal velocity in air, Royal Meteorological Society 96 (1970) 247-256.
- [22] R. Clift, J.R. Grace, M.E. Weber, Bubbles, drops and particles, Academic Press, 1978.
- [23] R. Gunn, G.D. Kinzer, The terminal velocity of fall for water droplets in stagnant air, Journal of Meteorology 6 (1949) 243-248.
- [24] M.A. Serio, F.G. Carollo, V. Ferro, Raindrop size distribution and terminal velocity for rainfall erosivity studies, A review. Journal of Hydrology 576 (2019) 210-228.
- [25] D.W. Green, M.Z. Southard, Perry's Chemical Engineers' Handbook, 9th Edition McGraw-Hill Education: New York, 2019.
- [26] D. Ambrose, C.H.S. Sprake, R. Townsend, Thermodynamic properties of organic oxygen compounds XXXIII. The vapour pressure of acetone, The Journal of Chemical Thermodynamics 6 (1974) 693-700.